

Optimizing Medical Image Segmentation with Advanced Decoder Design

Weibin Yang¹, Zhiqi Dong¹, Mingyuan Xu¹, Longwei Xu¹,
Dehua Geng¹, Yusong Li¹, Pengwei Wang^{1,*}

¹ School of Information Science and Engineering, Shandong University, Tsingtao,
266237, China

* Corresponding Author

E-mail: wangpw@sdu.edu.cn

October 2024

Abstract.

U-Net is widely used in medical image segmentation due to its simple and flexible architecture design. To address the challenges of scale and complexity in medical tasks, several variants of U-Net have been proposed. In particular, methods based on Vision Transformer (ViT), represented by Swin UNETR, have gained widespread attention in recent years. However, these improvements often focus on the encoder, overlooking the crucial role of the decoder in optimizing segmentation details. This design imbalance limits the potential for further enhancing segmentation performance. To address this issue, we analyze the roles of various decoder components, including upsampling method, skip connection, and feature extraction module, as well as the shortcomings of existing methods. Consequently, we propose Swin DER (i.e., Swin UNETR Decoder Enhanced and Refined) by specifically optimizing the design of these three components. Swin DER performs upsampling using learnable interpolation algorithm called offset coordinate neighborhood weighted up sampling (Oncampling) and replaces traditional skip connection with spatial-channel parallel attention gate (SCP AG). Additionally, Swin DER introduces deformable convolution along with attention mechanism in the feature extraction module of the decoder. Our model design achieves excellent results, surpassing other state-of-the-art methods on both the Synapse and the MSD brain tumor segmentation task.

Code is available at: <https://github.com/WillBeanYang/Swin-DER>

Keywords: Medical image segmentation, Upsampling, Transformer, Attention Mechanism, Deformable Convolution.

1. Introduction

Medical image segmentation aims to utilize computer technology to extract boundaries of anatomical or pathological features from medical images (Conze et al. 2023). Precise segmentation results can provide reliable volume and structural information of the target structure, thereby assisting clinicians in making accurate diagnostic and therapeutic

decisions(Zhang et al. 2024, Antonelli et al. 2022, Wasserthal et al. 2023). As an emerging biomedical image processing technique, medical image segmentation offers crucial support for intelligent diagnosis and precise medical care(Liu et al. 2021).

With the advancement of artificial intelligence, especially deep learning, medical image segmentation techniques based on deep convolutional neural networks (CNNs) have achieved noteworthy outcomes(Wang et al. 2022). Among these, U-Net (Ronneberger et al. 2015) has become one of the most extensively utilized architectures in medical image segmentation due to its optimized module design and flexibility(Azad et al. 2022). U-Net employs an encoder-decoder architecture, in which the encoder progressively extracts and compresses features, while the decoder is responsible for restoring spatial resolution and optimizing segmentation details(Siddique et al. 2021). Despite the powerful representational learning capability of CNN-based methods, the locality of convolution operations limits the network’s ability to learn long-distance dependencies(Shamshad et al. 2023).

Transformer(Dosovitskiy et al. 2020a) can encode long-distance dependencies and learn efficient feature representations. In the field of computer vision, the Vision Transformer (ViT)(Dosovitskiy et al. 2020b) slices images into patches, encoding them into a 1D sequence and using self-attention mechanism to capture the complex relationships between these patches. This effectively addresses the shortcomings of convolutional operations. Currently, many researchers are attempting to integrate the ViT into the improvement efforts of U-Net(Chen et al. 2021, Hatamizadeh et al. 2022, Cao et al. 2022), with Swin UNETR(Hatamizadeh et al. 2021) being the most prominent among them. Swin UNETR is distinguished by its incorporation of two sets of encoders that harness the individual strengths of both CNNs and transformers. This design grants it a powerful feature extraction capability, enabling it to achieve competitive segmentation performance across different datasets.

However, whether based on CNNs or Transformers, most current U-Net variants confine their improvement strategies to building more complex encoder, whereas leaving the decoder unchanged or adopting a simple symmetric structure. This imbalance in design is particularly evident in Swin UNETR, which has two sets of encoders while the decoder consists of simple Residual Blocks. We believe that there is still considerable room for improvement in the current decoder design. Firstly, commonly used upsampling methods often suffer from issues, such as checkerboard artifacts in transpose convolutions. Secondly, there is often a significant semantic gap between the encoder and decoder features that are simply merged through skip connections, which can negatively impact segmentation performance. Additionally, for objects with complex contours, convolution and transformer may struggle to precisely capture their boundary and shape features, thus affecting the ability of decoder to optimize segmentation details.

In response to these issues, we propose Swin DER (i.e., **Swin UNETR Decoder Enhanced and Refined**), which focuses on optimizing the decoder part of Swin UNETR. Our specific contributions are as follows:

- We propose a novel upsampling algorithm, **Offset coordinate neighborhood weighted upsampling (Onsampling)**, which optimizes interpolation algorithms using learnable position offsets and pixel weights.
- Introducing spatial and channel attention gates in parallel within skip connections to eliminate irrelevant and noisy responses in the skip connections.
- The decoder block is modified to a Deformable Squeeze-and-Attention (DSA) Block, utilizing deformable convolutions to further learn detailed features and focusing on important parts of the feature map through attention mechanisms.

Our model design achieves excellent results, surpassing other state-of-the-art methods on both the Synapse dataset(Landman et al. 2015) and brain tumor segmentation task in Medical Segmentation Decathlon (MSD)(Antonelli et al. 2022).

2. Related work

In this section, we review several optimization efforts aimed at the decoder components of the U-Net, including upsampling, skip connection, and feature extraction block. We also analyze the limitations of existing works.

2.1. Upsampling

Feature upsampling is one of the most critical operations in the decoder side of the U-Net architecture. Through upsampling, the U-Net progressively restores the resolution of feature maps to match the high-resolution supervision. Interpolation algorithms, such as nearest neighbor and bilinear interpolation, are the most commonly used methods for upsampling(Lehmann et al. 1999). These methods utilize the spatial distances between pixels to guide the upsampling process. However, due to following fixed rules to interpolate upsampled values, these algorithms fail to accurately capture the rich semantic information in medical images which are often characterized by diverse shapes and complex structures. To increase flexibility, some algorithms introduce learnable parameters in the upsampling process. For instance, transposed convolution(Noh et al. 2015) achieves upsampling by convolving the input feature map pixels with a convolutional kernel and adjusting the size of the output feature map according to the stride and padding parameters. However, when the stride and kernel size are not appropriately matched, transposed convolution can lead to checkerboard artifacts(Odena et al. 2016). W. Shi et al. proposed sub-pixel convolution(Shi, Caballero, Huszár, Totz, Aitken, Bishop, Rueckert & Wang 2016), which increases the depth of feature map channels through convolution operations and then moves the channel pixels to the spatial dimension to increase the feature map resolution. However, sub-pixel convolution is commonly used in super-resolution reconstruction tasks and does not perform well in semantic segmentation tasks. The literature (Shi, Caballero, Theis, Huszar, Aitken, Ledig & Wang 2016) also indicates that sub-pixel convolution

and transposed convolution essentially employ the same approach to processing low-resolution feature maps.

Unlike these learnable upsampling methods weigh pixels through convolution, we propose Onsampling, which achieves dynamic upsampling by learning offsets and neighborhood weights, effectively avoiding these issues.

2.2. Skip connection

Skip connections integrate deep semantic information with shallow local information, allowing the decoder to learn segmentation details more effectively(Drozdzal et al. 2016a). Moreover, skip connections also aid in the better convergence of the network(Szegedy et al. 2015). Zhou et al.(Zhou et al. 2019)introduced UNet++, which incorporates dense skip connections, allowing features from different levels to be aggregated instead of being confined to the same level of encoders and decoders. Huang et al.(Huang et al. 2020) believed that UNet++ still did not fully exploit full-scale features. In their architecture, UNet 3+, they further introduced full-scale skip connections, connecting each decoder with all encoders and all preceding decoders. Xiang et al.(Xiang et al. 2020) added backward skip connections on the basis of forward skip connections, transferring the features of decoder to encoder at the same level. These works increase the number of skip connections to make full use of features at each stage of the network, yet they neglect that the fusion of two sets of features with a large semantic gap could interfere with the learning process of the network(Ibtehaz & Rahman 2020). To eliminate irrelevant and noisy responses in skip connections, Okey et al. proposed Attention U-Net (Oktay et al. 2018), which employs attention gate (AG) to suppress encoder features that are irrelevant to the decoder features, reducing the semantic gap between the encoder and decoder features. However, AG merely adjusts the importance of encoder features in the spatial dimension, neglecting the semantic discrepancy between encoder and decoder across the channel dimension. To address this, we propose the spatial-channel parallel attention gate (SCP AG), which employs channel-wise attention gate to assign distinct spatial weight maps to each channel of encoder features.

2.3. Feature extraction block

After the decoder receives features concatenated via skip connection, it further merges these features through its feature extraction block, namely the decoder block, and gradually refines the details of the features. Typically, the decoder module consists of two consecutive convolution layers. Drozdzal et al.(Drozdzal et al. 2016a) proposed the Residual U-Net, employing residual blocks as the feature extraction blocks, which enabled the network to converge faster. Inspired by Inception blocks, Ibtehaz et al.(Ibtehaz & Rahman 2020) introduced the MultiRes block, adapting the Inception blocks concept by representing 5×5 and 7×7 convolutions as sequences of two and three 3×3 convolutions, respectively, and incorporating a residual connection with 1×1

convolution. With the rise of ViT in the field of computer vision, an increasing number of methods have started to utilize ViT as their feature extraction block (Hatamizadeh et al. 2022, Zhou et al. 2021). However, convolutions can only extract regular local features of objects, while ViT focuses more on capturing global features. Using them as feature extractors in decoders can not accurately capture the boundaries and detailed features of objects. The advent of deformable convolution (Dai et al. 2017) provides us with a new perspective. In deformable convolution, each position of the convolution kernel can dynamically offset based on the input data. These offsets are learned by the network, allowing the convolution kernel to adaptively adjust its shape to better match the local detail features of the input image. Consequently, we designed the Deformable Squeeze-and-Attention (DSA) Block as the feature extraction block for the decoder, replacing the second convolution layer in the Squeeze-and-Attention (SA) Block with deformable convolution.

3. Method

3.1. Overview

The overall architecture of Swin DER is illustrated in Figure 1. The network maintains an encoder-decoder structure similar to U-Net (Ronneberger et al. 2015). The encoder part of Swin DER is consistent with that of Swin UNETR (Hatamizadeh et al. 2021), comprising two sets based on different architectures: Transformer (Swin Transformer Block) and CNN (Residual Block). The Swin Transformer Block employs a sliding window self-attention mechanism to effectively integrate global information, while the Residual Block captures detailed and local structural information on this basis.

Our design focuses on the decoder side of the network. The decoder utilizes the Offset neighborhood weighted upsampling (Onsampling) algorithm for upsampling, which imparts learnable characteristics to the interpolation algorithm, enhancing its flexibility and effectively avoiding the checkerboard artifacts produced by transposed convolution. The feature maps outputted by encoder are not directly concatenated with the decoder features via skip connections. Instead, they first pass through the spatial-channel parallel attention gate (SCP AG). Under the guidance of decoder features, this process suppresses irrelevant parts between features in both spatial and channel dimensions. The concatenated features are finally sent to the Deformable Squeeze-and-Attention (DSA) Block for feature fusion and detail information learning. Additionally, we have introduced deep supervision during the training process, the outputs of different scales produced by each level of decoders after passing through the segmentation head are compared with their corresponding ground truth segmentation maps (after appropriate scaling) to calculate the loss.

The following sections will introduce these decoder components in detail.

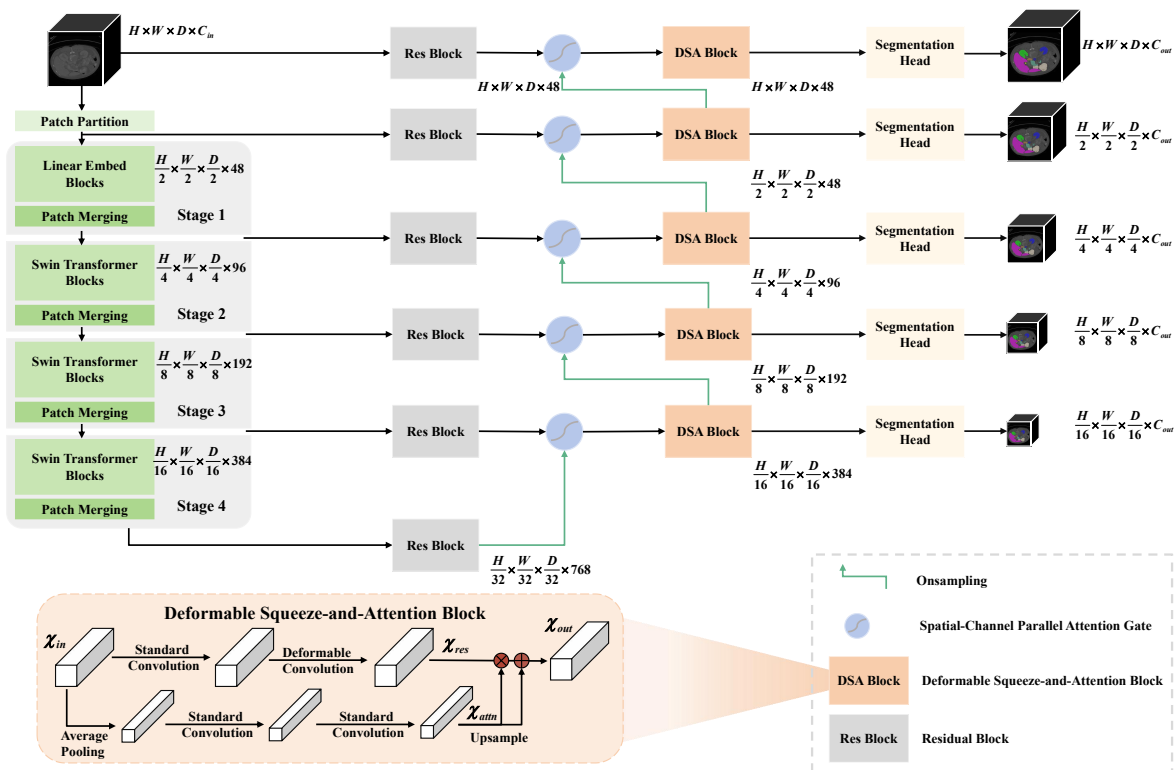


Figure 1. The overall architecture of our **Swin DER**. Our design focuses on the decoder side, the feature maps output by the second set of encoder (Residual Block) are reweighted in both spatial and channel dimensions through the **spatial-channel parallel attention gate** and concatenated in the channel dimension with decoder feature maps upsampled by **Onsampling** algorithm. Subsequently, the Deformable Squeeze-and-Attention (**DSA**) Block further integrates these features and utilizes the combined features to learn segmentation details.

3.2. Onsampling

Due to the fixed rules followed by interpolation algorithms in interpolating upsampled values, to increase flexibility, convolution-based upsampling algorithms such as transposed convolution (Noh et al. 2015) and sub-pixel convolution (Shi, Caballero, Huszár, Totz, Aitken, Bishop, Rueckert & Wang 2016) have been introduced. However, these algorithms often come with certain flaws, like the checkerboard artifacts (Odena et al. 2016) in transposed convolution. More importantly, we argue that in convolution-based upsampling algorithms, each output pixel is the weighted sum of pixels at corresponding positions across multiple channels. This design causes the output of each channel to be influenced not only by its own channel input but also by inputs from other channels, thereby affecting the clarity and distinctiveness of features in each channel.

Therefore, starting from interpolation algorithms, we designed a learnable interpolation algorithm named **Offset coordinate neighborhood weighted upsampling**

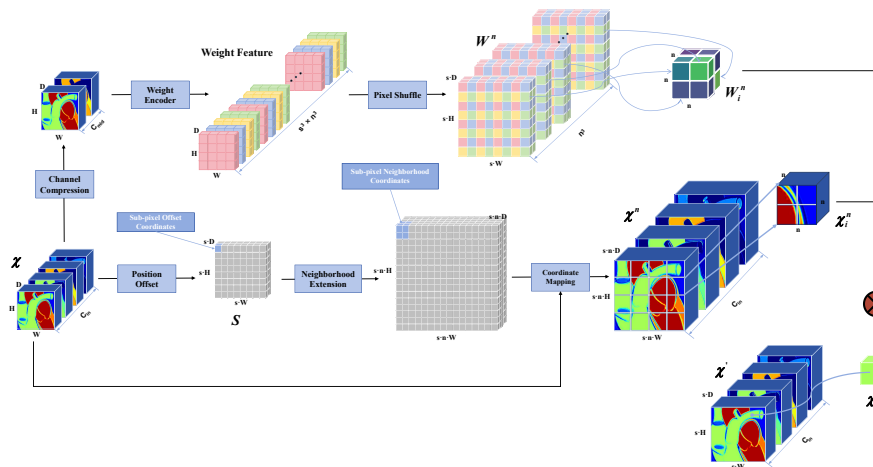


Figure 2. The computational process of Onsampling. Onsampling adds suitable offsets to the mapping coordinates in trilinear interpolation, enabling the learnability of sub-pixel positions. It obtains neighborhood weights through convolution, making the interpolation weights learnable. Ultimately, these weights are applied to the neighborhood pixels of the offset sub-pixels, realizing a dynamic interpolation algorithm.

(Onsampling). In traditional interpolation algorithms performing 2-fold upsampling, the sub-pixel positions are situated at the midpoint of the grid formed by the original pixels, and the value of a sub-pixel is derived through the weighted average of neighboring original pixel values, both the positions of sub-pixels and the weights of neighboring pixels are fixed and non-learnable. Onsampling introduces learnability to these two aspects, as illustrated in Figure 2.

For an input feature χ of size $H \times W \times D \times C_{in}$, when performing s -fold upsampling, the size of the corresponding original sub-pixel coordinate grid G is $s \cdot H \times s \cdot W \times s \cdot D \times 3$. Onsampling adds a learnable offset O to the original sub-pixel coordinates, calculated as follows:

$$O = 0.5 \cdot \text{Sigmoid}(\text{Conv}_1(x)) \cdot \text{Conv}_2(x) \quad (1)$$

The final sub-pixel coordinate grid S then becomes:

$$S = O + G \quad (2)$$

enabling dynamic changes in sub-pixel positions.

To learn the weights of the neighboring n original pixels of the sub-pixels, onsampling initially applies a $1 \times 1 \times 1$ convolution to compress the channels to C_{mid} . Subsequently, the compressed feature map undergoes encoding to produce the weight feature with dimensions $H \times W \times D \times C_w$, where $C_w = s^3 \times n^3$. After pixel shuffling and channel-wise softmax normalization, the final neighborhood weight map W^n is obtained.

By expanding the final sub-pixel coordinate grid to its n -neighborhood and mapping the input features, a neighborhood feature map χ^n is obtained. Multiplying and summing the i -th group of neighborhood features χ_i^n with its corresponding

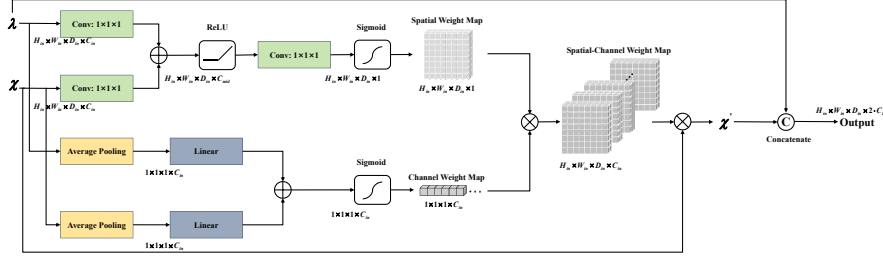


Figure 3. The schematic diagram of the spatial-channel parallel attention gate. Spatial-Channel Parallel Attention Gate computes weight maps separately in the spatial and channel dimensions, then merges these two-dimensional weight maps to form the spatial-channel weight map. Spatial-channel weight map is used to adjust the significance of each position and channel in the encoder feature map, thereby enhancing the model’s focus on important features and suppressing irrelevant information.

neighborhood weights W_i^n produces the value of the i -th pixel value in the output feature map χ'_i .

3.3. Spatial-Channel Parallel Attention Gate

Spatial-Channel Parallel Attention Gate dynamically adjusts the importance weights of encoder features in both the channel and spatial dimensions by learning the contextual information of the input features, as shown in Figure 3.

In the spatial dimension, encoder features χ and decoder features λ undergo $1 \times 1 \times 1$ convolution and are then added to generate spatial relevance features. After introducing non-linearity with *ReLU* activation, these spatial relevance features are compressed across channels through convolution and normalized to a range between 0 and 1 by the *sigmoid* function, ultimately generating the spatial weight map W_S of size $H_{in} \times W_{in} \times D_{in} \times 1$. The process is as follows:

$$W_S = \text{Sigmoid}(\text{Conv}(\text{ReLU}(\text{Conv}_\chi(\chi) + \text{Conv}_\lambda(\lambda)))) \quad (3)$$

In the channel dimension, χ and λ are processed with average pooling, reducing their dimensions to $1 \times 1 \times 1 \times C_{in}$ to obtain a global feature representation. The global features are processed through linear mapping and then added together to obtain channel relevance features. Finally, the channel relevance features are activated by the *sigmoid* function to create the channel weight map W_C . The calculation formula is as follows:

$$W_C = \text{Sigmoid}(\text{Linear}_\chi(\text{Avg}(\chi)) + \text{Linear}_\lambda(\text{Avg}(\lambda))) \quad (4)$$

W_S and W_C independently capture the spatial and channel correlation information within the input feature map. These two weight maps are generated in parallel and integrated together through element-wise multiplication to form the spatial-channel weight map W_{SC} :

$$W_{SC} = W_S \otimes W_c \quad (5)$$

where \otimes denotes element-wise multiplication.

Finally, the encoder feature maps are multiplied by the spatial-channel weight map to enhance the relevant features between the encoder and decoder. Through this mechanism, the spatial-channel parallel attention gate effectively minimizes the semantic gap between features.

3.4. Deformable Squeeze-and-Attention Block

The decoder is responsible for integrating features concatenated via skip connections and utilizing these concatenated features to refine segmentation details. Detail features are characterized by locality and irregular shapes. Deformable convolution (Dai et al. 2017) allows for the dynamic adjustment of the shape of convolution kernel to better adapt to the local features of the image, making it highly suitable for learning details.

The output $y(p_0)$ at position p_0 in standard convolution can be represented as:

$$y(p_0) = \sum_{p_n \subseteq R} w(p_n) \cdot x(p_0 + p_n) \quad (6)$$

where x is the input feature map, w represents the convolution weights, R denotes the convolutional receptive field, and p_n represents the relative positions within the convolution kernel. Deformable convolution dynamically computes offsets Δp_n for each position p_0 based on the input feature map through an additional convolutional network, making the output at position p_0 become:

$$y(p_0) = \sum_{p_n \subseteq R} w(p_n) \cdot x(p_0 + p_n + \Delta p_n) \quad (7)$$

The introduction of the Δp_n allows the convolution to transcend the constraints of a regular grid shape.

Based on deformable convolution, we propose the Deformable Squeeze-and-Attention (DSA) Block, as illustrated in Figure 1. In the DSA Block, the output feature map χ_{in} from the spatial-channel parallel attention gate first undergoes feature fusion through standard convolution. Subsequently, the block employs deformable convolution to learn the segmentation detail information of the fused features. This process can be represented as follows:

$$\chi_{res} = DefConv(Conv(\chi_{in})) \quad (8)$$

where $DefConv(\cdot)$ and $Conv(\cdot)$ respectively denote deformable convolution and standard convolution.

Simultaneously, χ_{in} undergoes incomplete average pooling and two consecutive convolutions, finally producing the attention map χ_{attn} through upsampling:

$$\chi_{attn} = Upsample(Conv_2(Conv_1(Avg(\chi_{in})))) \quad (9)$$

By multiplication with χ_{attn} , important parts in χ_{res} are highlighted. After reweighting, χ_{res} is combined with χ_{attn} through a residual connection, producing the output χ_{out} . The specific process is detailed as follows:

$$\chi_{out} = (\chi_{attn} \otimes \chi_{in}) \oplus \chi_{attn} \quad (10)$$

where \otimes represents element-wise multiplication, and \oplus denotes the residual connection.

3.5. Loss function

We train our networks with a combination of dice(Drozdal et al. 2016b) and cross-entropy loss, the total loss during the training phase can be formulated as follows:

$$L_{total} = w_1L_1 + w_2L_2 + w_3L_3 + w_4L_4 + w_5L_5 \quad (11)$$

where L_i , $i \in \{1, 2, 3, 4, 5\}$ represents the loss of the decoder at the i-th layer. When i equals 1, it represents the topmost decoder layer. Here, w_i denotes the weight of loss for the i-th layer of the encoder, the calculation formula is:

$$w_i = \frac{1}{2^{i-1}} \quad (12)$$

The loss for each decoder layer comprises dice loss and cross-entropy loss:

$$L = L_{dice} + L_{CE} \quad (13)$$

The computation formulas for dice loss and cross-entropy loss are as follows:

$$L_{dice} = 1 - \frac{2 \sum_{c=1}^C \sum_{i=1}^N g_i^c s_i^c}{\sum_{c=1}^C \sum_{i=1}^N g_i^c + \sum_{c=1}^C \sum_{i=1}^N s_i^c} \quad (14)$$

$$L_{CE} = -\frac{1}{N} \sum_{c=1}^C \sum_{i=1}^N g_i^c \log s_i^c \quad (15)$$

where C represents the number of categories and N represents the number of voxels in each category. g_i^c is the ground truth binary indicator of class label c of voxel i, and s_i^c is the corresponding segmentation prediction.

4. Experiments

4.1. Datasets

To validate the effectiveness of our method, we conducted experiments on Synapse multiorgan segmentation(Landman et al. 2015) and brain tumor segmentation task in Medical Segmentation Decathlon (MSD)(Antonelli et al. 2022). These datasets encompass different imaging modalities and segmentation tasks, providing a comprehensive evaluation of our model.

4.1.1. Synapse Dataset comprises abdominal CT scans from 30 subjects with manual annotations conducted under the supervision of radiologists from Vanderbilt University Medical Center, covering 8 distinct organs: spleen, right kidney, left kidney, gallbladder, liver, stomach, aorta, and pancreas. Each CT scan consists of 80 to 225 slices, and each slice having 512×512 pixels with a thickness varying from 1 to 6mm. Following the data split in (Chen et al. 2021), we select 18 samples for training our model and evaluated it on the remaining 12 samples.

4.1.2. MSD BraTS task This task is a part of the Medical Segmentation Decathlon (MSD)(Antonelli et al. 2022), focusing on the segmentation of brain tumors. It comprises 484 MRI images, each including four channels: FLAIR, T1w, T1gd, and T2w. The goal is to accurately label three sub-regions of the tumor: edema (ED), enhancing tumor (ET), and non-enhancing tumor (NET). The data originate from the Brain Tumor Segmentation (BraTS) challenges(Menze et al. 2014) in 2016 and 2017, where the complexity and heterogeneity of the segmentation targets pose significant challenges. Following the data split of UNETR(Hatamizadeh et al. 2022), the data is divided into 80% for training, 15% for validation, and 5% for testing. Moreover, to maintain consistency with reported results of other models, We display the segmentation result based on regions, which includes the whole tumor (WT), enhancing tumor (ET), and tumor core (TC). WT encompasses the entire volume of all tumor regions, while TC specifies the central area, excluding the edematous parts of the tumor.

4.2. Metrics

We have employed a comprehensive set of two evaluation metrics to rigorously assess the effectiveness of the methodology. These metrics consist of the Dice coefficient, utilized to quantitatively gauge the degree of similarity between the predicted segmentation and the ground truth segmentation. A value converging towards 1 signifies a higher degree of segmentation accuracy. Additionally, we have incorporated the Hausdorff 95 distance, a metric tailored to quantitatively capture the maximum spatial separation between the predicted segmentation and the ground truth. This parameter provides a robust evaluation of the alignment and coherence of segmentation boundaries. The expressions for the two evaluation metrics are provided below:

$$\text{Dice} = \frac{2 \sum_{i=1}^I Y_i \hat{Y}_i}{\sum_{i=1}^I Y_i + \sum_{i=1}^I \hat{Y}_i}, \quad (16)$$

$$HD_{95} = \max^{95^{th}} \left\{ \max_{y' \in Y'} \min_{\bar{y}' \in \bar{Y}'} \|y' - \bar{y}'\|, \max_{\bar{y}' \in \bar{Y}'} \min_{y' \in Y'} \|\bar{y}' - y'\| \right\}. \quad (17)$$

where Y and \bar{Y} denote the ground truth and prediction of voxel values. Y' and \hat{Y}' denote ground truth and prediction surface point sets. The notation $\max^{95^{th}}(\cdot)$ represents the value obtained by sorting in descending order and selecting the value corresponding to the 95th percentile.

4.3. Implementation details

We implement Swin DER in PyTorch(Paszke et al. 2019) 2.0.0 and nnU-Net 2.1.1. All experiments were conducted on NVIDIA GeForce RTX 3090 GPU with 24 GB memory. We follow the default data preprocessing, data augmentation, and training strategies of nnU-Net(Isensee et al. 2021). In the data pre-processing stage, we cropped all data to the non-zero regions, then the data will be resampled to the median voxel spacing of the dataset. In the presence of heterogeneous voxel spacings, meaning that the spacing along one axis is three times or more than that of the other axes, the 10 percentile of the spacing will be used as the spatial size for this axis. Finally, the data will be normalized. For CT images, such as synapse, the intensity values of the foreground portion of the dataset are first collected and the entire dataset is normalized by clipping to the [0.5, 99.5] percentiles of these intensity values. Z-score standard normalization(Zhang et al. 2021) then is applied to the data based on the mean and standard deviation of all the collected intensity values. For MRI images, such as MSD BraTS task, or other modalities, individual sample information is collected and z-score normalization is applied to that specific sample. Multiple techniques are employed for data augmentation, including rotation, scaling, Gaussian noise, Gaussian blur, brightness augmentation, contrast adjustment, simulation of low resolution, gamma transformation, and mirror transformation.

We set the patch size of the Synapse dataset to $128 \times 128 \times 64$, while for the MSD BraTS task, the patch size is set to $128 \times 128 \times 128$. The batch size for both datasets is 2. We utilize the cosine annealing strategy with warm-up to update the learning rate, setting the maximum learning rate to $3e-4$:

$$l_{cur} = \begin{cases} l_{initial} \times \frac{E_{cur}}{E_{warmup}}, & \text{if } E_{cur} < E_{warmup} \\ l_{initial} \times \left(1 + \cos\left(\pi \times \frac{E_{cur} - E_{warmup}}{E_{max} - E_{warmup}}\right)\right) / 2, & \text{if } E_{cur} \geq E_{warmup} \end{cases} \quad (18)$$

where l_{cur} denotes the learning rate of the current epoch, $l_{initial}$ is the maximum learning rate after the warm-up phase, E_{cur} denotes the number of current epochs, E_{warmup} is the epoch at which the warm-up ends, and E_{max} denotes the number of training epochs. During the training process, we set E_{max} to 1000 and E_{warmup} to 50. Furthermore, we employ the AdamW optimizer with weight decay of $3e-5$ to update gradients. We use the Dice Similarity Coefficient (DSC) and the 95% Hausdorff Distance (HD95) metrics to evaluate our model.

4.4. Quantitative results

To validate the effectiveness of Swin DER on different segmentation tasks, we compared our model with other state-of-the-art methods on the Synapse dataset and MSD BraTs Task. Table.1 shows the experimental results of all models on the multi-organ segmentation task. Swin DER achieved the highest average DSC and the lowest average HD95, reaching 86.68% and 8.64mm, respectively. Additionally, with the design of

Methods	Spl	RKid	LKid	Gal	Liv	Sto	Aor	Pan	Average	
									HD95 ↓	DSC ↑
U-Net (Ronneberger et al. 2015)	86.67	68.60	77.77	69.72	93.43	75.58	89.07	53.98	-	76.85
TransUNet (Chen et al. 2021)	85.08	77.02	81.87	63.16	94.08	75.62	87.23	55.86	31.69	77.49
Swin-UNet (Cao et al. 2022)	90.66	79.61	83.28	66.53	94.29	76.60	85.47	56.58	21.55	79.13
UNETR (Hatamizadeh et al. 2022)	85.00	84.52	85.60	56.30	94.57	70.46	89.80	60.47	18.59	78.35
MISSFormer (Huang et al. 2021)	91.92	82.00	85.21	68.65	94.41	80.81	86.99	65.67	18.20	81.96
Swin UNETR* (Hatamizadeh et al. 2021)	88.81	85.84	86.43	65.87	95.54	75.96	89.77	69.92	15.19	82.27
nnFormer (Zhou et al. 2021)	90.51	86.25	86.57	70.17	96.84	86.83	92.04	83.35	10.63	86.57
Swin DER(Ours)	92.41	87.21	87.48	74.63	96.24	82.43	92.65	80.36	8.64	86.68

Table 1. Comparison on the abdominal multi-organ Synapse dataset. We use HD95 and DSC to evaluate the performance of each model. Experimental results of baselines refer to nnFormer(Zhou et al. 2021). The best results are indicated in bold. * indicates that the baseline is implemented by ourselves. Swin DER achieved the best performance. Abbreviations stand for: Spl: *spleen*, RKid: *right kidney*, LKid: *left kidney*, Gal: *gallbladder*, Liv: *liver*, Sto: *stomach*, Aor: *aorta*, Pan: *pancreas*.

decoder, Swin DER significantly enhances network performance over Swin UNETR, increasing the average DSC by 4.41% and reducing the average HD95 by 9.55mm. Compared to second-best method nnFormer, we significantly improved the segmentation performance of the spleen, right kidney, left kidney, gallbladder, and aorta, with DSC improvements of 1.9%, 0.85%, 0.91%, 4.46%, and 0.61%, respectively.

Fig.4 illustrates the qualitative comparison between Swin DER and other methods on the Synapse dataset. As shown in the first row, our method improves the segmentation quality of the stomach. In the second row, nnFormer exhibits over-segmentation of the spleen, which contaminates the segmentation results of the stomach, while both Swin UNETR and UNETR suffer from under-segmentation of the stomach. Swin DER provides a complete segmentation of the stomach and clearly distinguishes the boundary between the stomach and the spleen. In the third row, other methods exhibit varying degrees of under-segmentation of the gallbladder. Additionally, Swin UNETR suffers from severe over-segmentation of the spleen. Only Swin DER provides a complete segmentation of the gallbladder. The fourth row demonstrates Swin DER does not segment a non-existent gallbladder compared to other methods.

Table.2 presents the comparative experimental results on the MSD brain tumor segmentation task, our model achieved the best average DSC and HD95, which are respectively of 86.99% and 3.65mm. Compared to the baseline model Swin UNETR, the average DSC increased by 1.25%, and the average HD95 decreased by 0.14 mm. Additionally, Swin DER outperformed the second-ranked method nnFormer in both evaluation metrics across all parts of the brain tumor and in the overall average results.

Fig.5 illustrates the visualization results, in the first line, all methods except Swin DER exhibited under-segmentation of the enhancing tumor. In the second row, both nnFormer and Swin UNETR exhibited over-segmentation of the non-enhancing tumor and under-segmentation of the enhancing tumor. Additionally, compared to UNETR, my method more clearly distinguished the boundaries between the two part. The third row shows the segmentation results of edema using by different methods. It can be

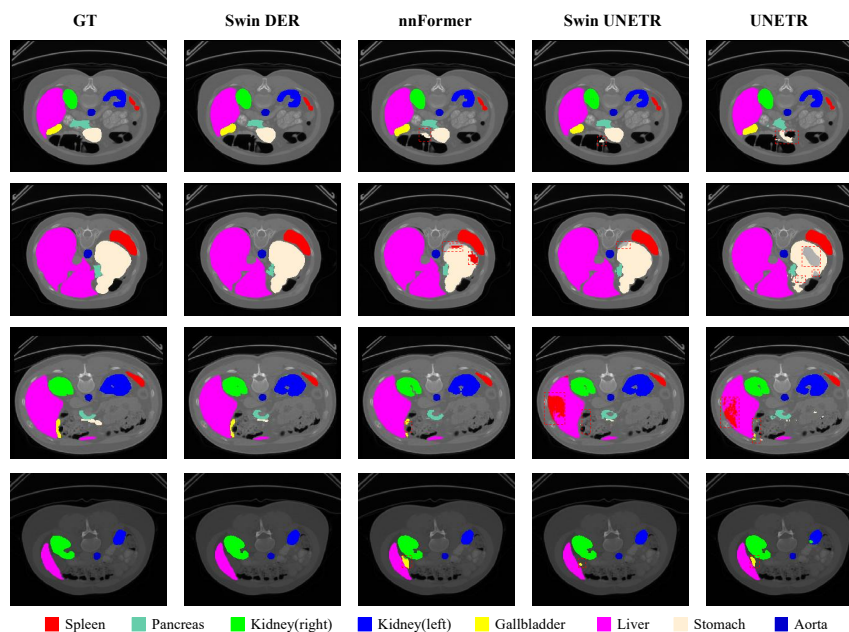


Figure 4. Visualization results of multi-organ segmentation on the Synapse dataset. We primarily compare Swin DER with other transformer-based segmentation models, such as UNETR, Swin UNETR, and nnFormer.

observed that nnFormer and UNETR exhibited over-segmentation, while Swin UNETR exhibited under-segmentation. Only Swin DER achieved accurate segmentation of edema. In the fourth row, all methods except Swin DER exhibited under-segmentation of the non-enhancing tumor. Additionally, UNETR also over-segmented the enhancing tumor.

Methods	WT		ET		TC		Average	
	HD95 ↓	DSC ↑	HD95 ↓	DSC ↑	HD95 ↓	DSC ↑	HD95 ↓	DSC ↑
SETR NUP (Zheng et al. 2021)	14.419	69.7	11.72	54.4	15.19	66.9	13.78	63.7
SETR PUP (Zheng et al. 2021)	15.245	69.6	11.76	54.9	15.023	67.0	14.01	63.8
SETR MLA (Zheng et al. 2021)	15.503	69.8	10.24	55.4	14.72	66.5	13.49	63.9
TransUNet (Chen et al. 2021)	14.03	70.6	10.42	54.2	14.5	68.4	12.98	64.4
TransBTS (Wenxuan et al. 2021)	10.03	77.9	9.97	57.4	8.95	73.5	9.65	69.6
CoTr w/o CNN encoder (Xie et al. 2021)	11.49	71.2	9.59	52.3	12.58	69.8	11.22	64.4
CoTr (Xie et al. 2021)	9.20	74.6	9.45	55.7	10.45	74.8	9.70	68.3
UNETR (Hatamizadeh et al. 2022)	8.27	78.9	9.35	58.5	8.85	76.1	8.82	71.1
Swin UNETR* (Hatamizadeh et al. 2021)	3.77	91.33	2.65	80.76	4.95	85.12	3.79	85.74
nnFormer (Zhou et al. 2021)	3.80	91.3	3.87	81.8	4.49	86.0	4.05	86.4
Swin DER(Ours)	3.65	92.27	2.94	82.59	4.36	86.10	3.65	86.99

Table 2. Comparison on the brain tumor segmentation task in Medical Segmentation Decathlon. We use HD95 and DSC to evaluate the performance of each model. Experimental results of baselines refer to nnFormer(Zhou et al. 2021). The best results are indicated in bold. * indicates that the baseline is implemented by ourselves. Swin DER achieved the best performance. Abbreviations stand for: WT: *whole tumor*, ET: *enhancing tumor*, TC: *tumor core*.

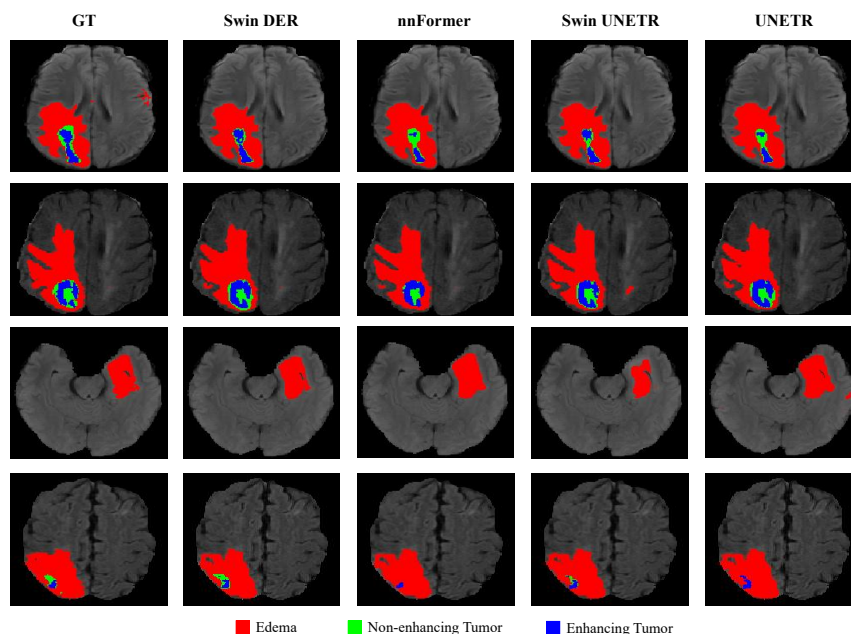


Figure 5. Brain tumor segmentation visualization. Compared to the current state-of-the-art image segmentation methods, Swin DER achieved the best results.

4.5. Ablation study

4.5.1. Module ablation experiments We conducted ablation experiments on the proposed module using the Synapse dataset, with DSC as the default evaluation metric. Table 3 displays the detailed experimental results.

The first row in the table represents the baseline model Swin UNETR (Hatamizadeh et al. 2021). It can be observed that Swin UNETR achieves good segmentation performance on the Synapse dataset, attributed to its complex encoder. However, due to the relatively simple and coarse design of the decoder, its performance on smaller organs like the gallbladder and pancreas is less than ideal with the average DSC lagging behind the current best model nnFormer (Zhou et al. 2021) by 4.3%, as shown in Table 1.

We first replaced the upsampling method in the decoder with Onsampling. Onsampling achieves dynamic interpolation by learning positional offsets and neighborhood weights, effectively improving segmentation performance. As shown in the second row of Table 3, compared to using transposed convolution for upsampling, the average DSC increased by 1.7%, with a significant improvement in the segmentation of the gallbladder and pancreas, where DSC increased by 5.6% and 4.03%, respectively.

Next, we introduced the spatial-channel parallel attention gate, which learns the weights of encoder features within the skip connections in the channel and spatial dimensions. As shown in the third row of Table 3, this operation further improved overall performance by 1.01 percents. This indicates that the spatial-channel parallel attention gate effectively bridges the semantic gap between encoder and decoder

Models	Spl	RKid	LKid	Gal	Liv	Sto	Aor	Pan	Average
Encoder + Res Block + Trans Conv (Swin UNETR (Hatamizadeh et al. 2021))	88.81	85.84	86.43	65.87	95.54	75.96	89.77	69.92	82.27
Encoder + Res Block + Onsampling	88.01	85.84	87.14	71.47	95.16	78.47	91.69	73.95	83.97
Encoder + Res Block + SCP AG + Onsampling	93.09	86.07	87.44	71.81	96.04	79.33	90.47	75.56	84.98
Encoder + DSA Block + SCP AG + Onsampling (Swin DER)	92.41	87.21	87.48	74.63	96.24	82.43	92.65	80.36	86.68

Table 3. Investigation of the impact of different modules used in Swin DER. Each module in our architecture plays a critical role in enhancing the quality of segmentation. **Encoder** represents the encoder of Swin UNETR(Hatamizadeh et al. 2021). **Res Block** denotes the use of a residual block as the decoder module. **Trans Conv** represents the use of transposed convolution for upsampling. **SCP AG** denotes the incorporation of spatial-channel parallel attention gate within the skip connections. **Onsampling** represents the use of offset coordinate neighborhood weighted upsampling for the upsampling process. **DSA Block** indicates the use of Deformable Squeeze-and-Attention as the decoder module.

features, significantly enhancing the skip connections.

Finally, we replaced the feature extraction module on the decoder side with the DSA Block, which further enhanced the performance of model, increasing the average DSC by an additional 1.7%. As shown in Table 1, combining these three modules to specifically improve various parts of the decoder enabled Swin DER to surpass nnFormer, establishing it as the new state-of-the-art model.

4.5.2. Comparison of different upsampling methods The quantitative experiment results of different upsampling methods are shown in Table 4. Onsampling achieved the highest average DSC of 86.68% on the Synapes dataset.

Trilinear Interpolation follows fixed rules, which limits its ability to adapt to the complexity and variability of medical images. As a result, it achieved the lowest average DSC of 85.06%. Transposed convolution performs upsampling by learning the parameters of convolutional kernels, allowing it to automatically adjust these parameters during training to suit specific tasks. Compared to trilinear interpolation, the use of transposed convolution increased the average DSC by 0.69 percents. However, if not designed properly, it may introduce checkerboard artifacts during the upsampling process. Sub-pixel convolution performs convolution operations on low-resolution feature maps to generate multi-channel feature maps, and then uses pixel shuffle to rearrange these channels into a higher-resolution space. The experimental results in Table 4 shows that there is no significant performance improvement compared to transposed convolution. Additionally, Shi et al.(Shi, Caballero, Theis, Huszar, Aitken, Ledig & Wang 2016) have theoretically demonstrated that sub-pixel convolution and transposed convolution do not have substantial differences in their algorithmic essence.

Compared to transposed convolution and sub-pixel convolution, onsampling does not place learnable parameters on the convolution. Instead, it learns the positional offsets and weights of the interpolation reference points, endowing the interpolation algorithm with learnable capabilities and overcoming the shortcomings of convolution-based upsampling methods.

Method	Spl	RKid	LKid	Gal	Liv	Sto	Aor	Pan	Average
Trilinear Interpolation	87.08	87.36	87.08	70.59	95.48	82.08	91.44	79.34	85.06
Transposed Convolution	87.92	87.23	87.23	73.11	95.33	82.17	92.08	80.93	85.75
Sub-pixel Convolution	88.45	86.71	87.42	73.70	95.85	83.31	92.09	79.01	85.82
Onsampling	92.41	87.21	87.48	74.63	96.24	82.43	92.65	80.36	86.68

Table 4. Ablation experiments on upsampling methods.

4.5.3. Comparison of attention gate The relevant experimental results of the attention gate are shown in Table 5. When the encoder and decoder feature maps are directly concatenated without using the AG, the semantic gap between the low-level detail information of the encoder features and the high-level semantic information of the decoder features negatively impacts the segmentation performance, resulting in an average DSC of only 85.56%. The AG reweights the encoder features spatially based on the decoder features, partially bridging the semantic gap between them, which improves the average DSC by 0.2 percents. SCP AG further learns the weights in the channel dimension and combining them with spatial weights to reweight the decoder features across both dimensions, achieving the best average DSC of 86.68%.

Method	Spl	RKid	LKid	Gal	Liv	Sto	Aor	Pan	Average
No Attention Gate	87.22	87.39	87.18	74.45	95.42	82.36	91.59	78.84	85.56
Attention Gate	92.21	86.37	87.15	73.19	95.31	82.13	92.23	77.49	85.76
Spatial-Channel Parallel Attention Gate	92.41	87.21	87.48	74.63	96.24	82.43	92.65	80.36	86.68

Table 5. Ablation experiments on the attention gate of skip connection.

4.5.4. Comparison of feature extraction module of decoder The ablation experiment results for the decoder feature extraction module are shown in Table 6, where the Basic Block represents two consecutive convolution layers. The residual block, through additional connections, reduces the risk of overfitting and enhances the generalization ability of model. Compared to the basic block, it improved the average DSC by 0.24%. Deformable convolution(Dai et al. 2017) can adaptively adjust sampling positions, allowing it to better preserve and utilize important information when dealing with complex spatial structures. The results in the fourth and fifth rows of the Table 6 show that after replacing the second convolution layer in both the residual block and the basic block with deformable convolution, the average DSC increased by 0.31 and 0.12 percentage points respectively. The DSA Block introduces attention mechanism into the additional connection of the residual module with deformable convolution, assigning higher weight to important features and providing guidance for the feature extraction module, achieving the best segmentation results.

Method	Spl	RKid	LKid	Gal	Liv	Sto	Aor	Pan	Average
Basic Block	89.54	87.19	87.51	67.85	95.57	81.79	91.40	77.04	84.74
Res Block	93.09	86.07	87.44	71.81	96.04	79.33	90.47	75.56	84.98
Basic Block with Deformable Conv	87.76	87.38	87.60	70.86	95.59	80.02	92.18	77.52	84.86
Res Block with Deformable Conv	87.67	87.07	87.27	72.82	95.35	81.54	90.87	79.72	85.29
DSA Block	92.41	87.21	87.48	74.63	96.24	82.43	92.65	80.36	86.68

Table 6. Ablation experiments on the feature extraction module of the decoder.

5. Conclusion

In this paper, we propose a network focused on decoder design, called Swin DER. Swin DER enhances the upsampling process, skip connection, and decoder feature extraction module. We design a novel and efficient upsampling method called Onsampling, which improves the flexibility and scalability of the interpolation algorithm by learning the positional offsets and weights of neighboring pixels. Onsampling also avoids the drawbacks of convolution-based upsampling methods. For skip connection, we introduce a spatial-channel parallel attention gate, which weights the encoder features across both spatial and channel dimensions. This helps bridge the significant semantic gap between the encoder and decoder features. Additionally, we introduce deformable convolution and attention mechanism into the feature extraction module. This combination allows the decoder to dynamically adjust its receptive field while giving more focus to important features, thereby enhancing the feature extraction and learning capabilities of decoder.

Experimental results show that on both the Synapse and the MSD brain tumor segmentation task, Swin DER outperforms other state-of-the-art methods, particularly those based on transformer. This proves the superiority of our method. More importantly, it demonstrates that optimizing the decoder can further enhance segmentation capability of model.

6. Acknowledge

This work was supported by National Natural Science Foundation of China under Grant 61301253 and the Major Scientific and Technological Innovation Project in Shandong Province under Grant 2021CXG010506 and 2022CXG010504; "New Universities 20 items" Funding Project of Jinan under Grant 2021GXRC108 and 2021GXRC024.

References

- Antonelli M, Reinke A, Bakas S, Farahani K, Kopp-Schneider A, Landman B A, Litjens G, Menze B, Ronneberger O, Summers R M et al. 2022 *Nature communications* **13**(1), 4128.
- Azad R, Aghdam E K, Rauland A, Jia Y, Avval A H, Bozorgpour A, Karimijafarbigloo S, Cohen J P, Adeli E & Merhof D 2022 *arXiv preprint arXiv:2211.14830*.
- Cao H, Wang Y, Chen J, Jiang D, Zhang X, Tian Q & Wang M 2022 *in 'European conference on computer vision'* Springer pp. 205–218.

- Chen J, Lu Y, Yu Q, Luo X, Adeli E, Wang Y, Lu L, Yuille A L & Zhou Y 2021 *arXiv preprint arXiv:2102.04306* .
- Conze P H, Andrade-Miranda G, Singh V K, Jaouen V & Visvikis D 2023 *IEEE Transactions on Radiation and Plasma Medical Sciences* .
- Dai J, Qi H, Xiong Y, Li Y, Zhang G, Hu H & Wei Y 2017 in ‘Proceedings of the IEEE international conference on computer vision’ pp. 764–773.
- Dosovitskiy A, Beyer L, Kolesnikov A, Weissenborn D, Zhai X, Unterthiner T, Dehghani M, Minderer M, Heigold G, Gelly S et al. 2020a *arXiv preprint arXiv:2010.11929* .
- Dosovitskiy A, Beyer L, Kolesnikov A, Weissenborn D, Zhai X, Unterthiner T, Dehghani M, Minderer M, Heigold G, Gelly S et al. 2020b *arXiv preprint arXiv:2010.11929* .
- Drozdzal M, Vorontsov E, Chartrand G, Kadoury S & Pal C 2016a in ‘International workshop on deep learning in medical image analysis, international workshop on large-scale annotation of biomedical data and expert label synthesis’ Springer pp. 179–187.
- Drozdzal M, Vorontsov E, Chartrand G, Kadoury S & Pal C 2016b in ‘International Workshop on Deep Learning in Medical Image Analysis, International Workshop on Large-Scale Annotation of Biomedical Data and Expert Label Synthesis’ Springer pp. 179–187.
- Hatamizadeh A, Nath V, Tang Y, Yang D, Roth H R & Xu D 2021 in ‘International MICCAI Brainlesion Workshop’ Springer pp. 272–284.
- Hatamizadeh A, Tang Y, Nath V, Yang D, Myronenko A, Landman B, Roth H R & Xu D 2022 in ‘Proceedings of the IEEE/CVF winter conference on applications of computer vision’ pp. 574–584.
- Huang H, Lin L, Tong R, Hu H, Zhang Q, Iwamoto Y, Han X, Chen Y W & Wu J 2020 in ‘ICASSP 2020-2020 IEEE international conference on acoustics, speech and signal processing (ICASSP)’ IEEE pp. 1055–1059.
- Huang X, Deng Z, Li D & Yuan X 2021 *arXiv preprint arXiv:2109.07162* .
- Ibtehaz N & Rahman M S 2020 *Neural networks* **121**, 74–87.
- Isensee F, Jaeger P F, Kohl S A, Petersen J & Maier-Hein K H 2021 *Nature methods* **18**(2), 203–211.
- Landman B, Xu Z, Igelsias J, Styner M, Langerak T & Klein A 2015 in ‘Proc. MICCAI Multi-Atlas Labeling Beyond Cranial Vault—Workshop Challenge’ Vol. 5 p. 12.
- Lehmann T M, Gonner C & Spitzer K 1999 *IEEE transactions on medical imaging* **18**(11), 1049–1075.
- Liu X, Song L, Liu S & Zhang Y 2021 *Sustainability* **13**(3), 1224.
- Menze B H, Jakab A, Bauer S, Kalpathy-Cramer J, Farahani K, Kirby J, Burren Y, Porz N, Slotboom J, Wiest R et al. 2014 *IEEE transactions on medical imaging* **34**(10), 1993–2024.
- Noh H, Hong S & Han B 2015 in ‘Proceedings of the IEEE international conference on computer vision’ pp. 1520–1528.
- Odena A, Dumoulin V & Olah C 2016 *Distill* **1**(10), e3.
- Oktay O, Schlemper J, Folgoc L L, Lee M, Heinrich M, Misawa K, Mori K, McDonagh S, Hammerla N Y, Kainz B et al. 2018 *arXiv preprint arXiv:1804.03999* .
- Paszke A, Gross S, Massa F, Lerer A, Bradbury J, Chanan G, Killeen T, Lin Z, Gimelshein N, Antiga L, Desmaison A, Kopf A, Yang E, DeVito Z, Raison M, Tejani A, Chilamkurthy S, Steiner B, Fang L, Bai J & Chintala S 2019 in H Wallach, H Larochelle, A Beygelzimer, F d'Alché-Buc, E Fox & R Garnett, eds, ‘Advances in Neural Information Processing Systems 32’ Curran Associates, Inc. pp. 8024–8035.
URL: <http://papers.neurips.cc/paper/9015-pytorch-an-imperative-style-high-performance-deep-learning-library.pdf>
- Ronneberger O, Fischer P & Brox T 2015 in ‘Medical Image Computing and Computer-Assisted Intervention—MICCAI 2015: 18th International Conference, Munich, Germany, October 5-9, 2015, Proceedings, Part III 18’ Springer pp. 234–241.
- Shamshad F, Khan S, Zamir S W, Khan M H, Hayat M, Khan F S & Fu H 2023 *Medical Image Analysis* p. 102802.
- Shi W, Caballero J, Huszár F, Totz J, Aitken A P, Bishop R, Rueckert D & Wang Z 2016 in ‘Proceedings

- of the IEEE conference on computer vision and pattern recognition' pp. 1874–1883.
- Shi W, Caballero J, Theis L, Huszar F, Aitken A, Ledig C & Wang Z 2016 *arXiv preprint arXiv:1609.07009* .
- Siddique N, Paheding S, Elkin C P & Devabhaktuni V 2021 *Ieee Access* **9**, 82031–82057.
- Szegedy C, Liu W, Jia Y, Sermanet P, Reed S, Anguelov D, Erhan D, Vanhoucke V & Rabinovich A 2015 *in* 'Proceedings of the IEEE conference on computer vision and pattern recognition' pp. 1–9.
- Wang R, Lei T, Cui R, Zhang B, Meng H & Nandi A K 2022 *IET Image Processing* **16**(5), 1243–1267.
- Wasserthal J, Breit H C, Meyer M T, Pradella M, Hinck D, Sauter A W, Heye T, Boll D T, Cyriac J, Yang S et al. 2023 *Radiology: Artificial Intelligence* **5**(5).
- Wenxuan W, Chen C, Meng D, Hong Y, Sen Z & Jiangyun L 2021 *in* 'International Conference on Medical Image Computing and Computer-Assisted Intervention, Springer' pp. 109–119.
- Xiang T, Zhang C, Liu D, Song Y, Huang H & Cai W 2020 *in* 'Medical Image Computing and Computer Assisted Intervention–MICCAI 2020: 23rd International Conference, Lima, Peru, October 4–8, 2020, Proceedings, Part I 23' Springer pp. 74–84.
- Xie Y, Zhang J, Shen C & Xia Y 2021 *in* 'Medical Image Computing and Computer Assisted Intervention–MICCAI 2021: 24th International Conference, Strasbourg, France, September 27–October 1, 2021, Proceedings, Part III 24' Springer pp. 171–180.
- Zhang C, Hua Q, Chu Y & Wang P 2021 *Computers in Biology and Medicine* **133**, 104424.
- Zhang Y, Shen Z & Jiao R 2024 *Computers in Biology and Medicine* p. 108238.
- Zheng S, Lu J, Zhao H, Zhu X, Luo Z, Wang Y, Fu Y, Feng J, Xiang T, Torr P H et al. 2021 *in* 'Proceedings of the IEEE/CVF conference on computer vision and pattern recognition' pp. 6881–6890.
- Zhou H Y, Guo J, Zhang Y, Yu L, Wang L & Yu Y 2021 *arXiv preprint arXiv:2109.03201* .
- Zhou Z, Siddiquee M M R, Tajbakhsh N & Liang J 2019 *IEEE transactions on medical imaging* **39**(6), 1856–1867.